## BIOMATERIALS

# A three-dimensionally architected electronic skin mimicking human mechanosensation

Zhi Liu[1,2]†, Xiaonan Hu[1,2]†, Renheng Bo[1,2]†, Youzhou Yang[1,2], Xu Cheng[1,2,3,4], Wenbo Pang[1,2], Qing Liu[1,2], Yuejiao Wang[1,2], Shuheng Wang[1,2], Shiwei Xu[1,2], Zhangming Shen[1,2], Yihui Zhang[1,2]*

Human skin sensing of mechanical stimuli originates from transduction of mechanoreceptors that converts external forces into electrical signals. Although imitating the spatial distribution of those mechanoreceptors can enable developments of electronic skins capable of decoupled sensing of normal/shear forces and strains, it remains elusive. We report a three-dimensionally (3D) architected electronic skin (denoted as 3DAE-Skin) with force and strain sensing components arranged in a 3D layout that mimics that of Merkel cells and Ruffini endings in human skin. This 3DAE-Skin shows excellent decoupled sensing performances of normal force, shear force, and strain and enables development of a tactile system for simultaneous modulus/curvature measurements of an object through touch. Demonstrations include rapid modulus measurements of fruits, bread, and cake with various shapes and degrees of freshness.

Humans can accomplish dexterous manipulation, environmental exploration, and perception of physical properties of touched objects, among other tactile tasks as a result of skin's decoupled sensing capabilities of multimodal mechanical stimuli and the brain's learning and processing capabilities of perceived signals. Biological studies showed that our skin's sense of mechanical stimuli originates from the transduction of mechanoreceptors in the skin (1–3), which converts the forces applied to the skin into electrical signals that propagate to the central nervous system (CNS) through the axons. Merkel cells and Ruffini endings are two types of slowly adapting mechanoreceptors, which reside at the bottom of the epidermis and within the dermis, respectively, with a densely distributed array in three-dimensional (3D) space (4–7). Because Merkel cells—supported by collagen fiber networks in the dermis—are very close to the skin surface, they are highly sensitive to the forces applied to the skin as the induced stress decays rapidly from the loading region (4, 5). In comparison to Merkel cells, Ruffini endings are distributed much farther from the skin surface and therefore are not as sensitive to external forces (e.g., pressure) even when the skin itself is stretched (6, 7). As a result of such 3D distribution of mechanoreceptors (Fig. 1A, left), Merkel cells and Ruffini endings can effectively perceive the external forces and the strain of the skin, respectively.

Imitating the above spatial distribution of mechanoreceptors in the skin can enable developments of artificial electronic skins capable of decoupled sensing of normal/shear forces and strains, but remains highly challenging, due to the difficulties in realizing a complexly architected 3D electronic device with well-controlled 3D distributions of sensing components. Although many inspiring and exciting developments of electronic skins have been reported, such as epidermal electronics (8, 9), neuromorphic skin electronic systems (10–13), skin-integrated electronic systems (14, 15), electronic skins with intrinsically stretchable electronic components (16–19), and electronic skins for multiparameter sensing (20–23) and haptic interfaces (24–27), none of them have imitated the 3D spatial distribution of mechanoreceptors. Additionally, decoupled measurements of normal force, shear force, and tensile strain, at a spatial resolution close to human skin, also remains elusive.

We report a bioinspired design of 3D architected electronic skin (denoted as 3DAE-Skin) adopting a skin-like multilayer construction, where force and strain sensing components are arranged in a 3D layout that mimics that of Merkel cells and Ruffini endings in the skin (Fig. 1A). Microfabrication techniques allow formation of a lithographically defined multilayered electronic device consisting of laminated force and strain sensing arrays, which was transformed into biomimetic 3D configuration through precisely controlled mechanical assembly (28–30). A heterogeneous encapsulation strategy of the 3D architected device ensures that the surrounding soft materials of force and strain sensing components have similar mechanical properties to those of Merkel cells and Ruffini endings in the skin. Experimental and theoretical studies of 3DAE-Skin show excellent decoupled sensing performances of normal force, shear force, and strain. A tactile system based on 3DAE-Skin, data acquisition circuits, and deep learning aided signal processing module is developed, which can simultaneously measure the elastic modulus and local principal curvature components of an object through a simple touch.

### Bioinspired design and fabrication of the 3DAE-Skin

Figure 1A presents the bioinspired design concept of the 3DAE-Skin. Similar to the tri-layer construction of skin, the 3DAE-Skin consists of three layers: "epidermis," "dermis," and "hypodermis." The thickness and elastic modulus of those layers are close to those of the skin (table S1): ~145 μm and ~436 kPa (epidermis), ~600 μm and ~107 kPa (dermis), and ~4.5 mm and ~52 kPa (hypodermis). The sensing components and associated electrical circuits are embedded mainly in the dermis layer and the signals generated from sensing components are collected and processed through modules of data acquisition and deep learning aided signal processing, similar to the function of the CNS (fig. S1).

Figure 1, B and C, shows an expanded view of the geometric layout of the 3DAE-Skin and its representative functional unit. The 3DAE-Skin consists of three parts: functional, substrate, and encapsulation. The functional part encompasses an array (5 × 5) of 3D structured units, which are interconnected with the connection pad. Each of the 3D functional unit adopts a nine-layer construction (Fig. 1C and figs. S2 and S3), including two force sensing layers (5 nm Cr / 60 nm Au), two strain sensing layers (5 nm Cr / 60 nm Au), and five polyimide (PI) layers (1.2 μm for the top and bottom layers, and 0.8 μm for all the other layers) that encase each of the sensing layers. Microfabrication techniques (see Materials and Methods and figs. S4 and S5 for details) allow manufacturing of such multilayered electronic device in pre-defined planar layout. Transfer printing and mechanically guided assembly (figs. S6 and S7) enable transformation of the 2D electronic device into desired 3D configuration on top of the elastomeric substrate [a bilayer of Dragon Skin (10 Slow, Smooth-On, Easton, PA, US; mix ratio = 1:1; elastic modulus ~150 kPa; ~0.5 mm) and Ecoflex (00-20, Smooth-On, Easton, PA, US; mix ratio = 1:5; elastic modulus ~40 kPa; ~4 mm)]. In particular, a distributed 3D architecture is adopted to ensure different distances of force and strain sensing components (i.e., piezoresistive sensors) from the surface of 3DAE-Skin, where force sensing components are arranged on eight-armed cage mesostructures with a relatively large height (~600 μm) whereas strain sensing components are located on arch mesostructures with a smaller height (~250 μm). The eight-armed cage mesostructure

[1]Applied Mechanics Laboratory, Department of Engineering Mechanics, Tsinghua University, Beijing 100084, P.R. China. [2]Laboratory of Flexible Electronics Technology, Tsinghua University, Beijing 100084, P.R. China. [3]Department of Materials Science and Engineering, National University of Singapore, Singapore 119276, Singapore. [4]Institute for Health Innovation & Technology (iHealthtech), National University of Singapore, Singapore 119276, Singapore.
*Corresponding author. Email: yihuizhang@tsinghua.edu.cn
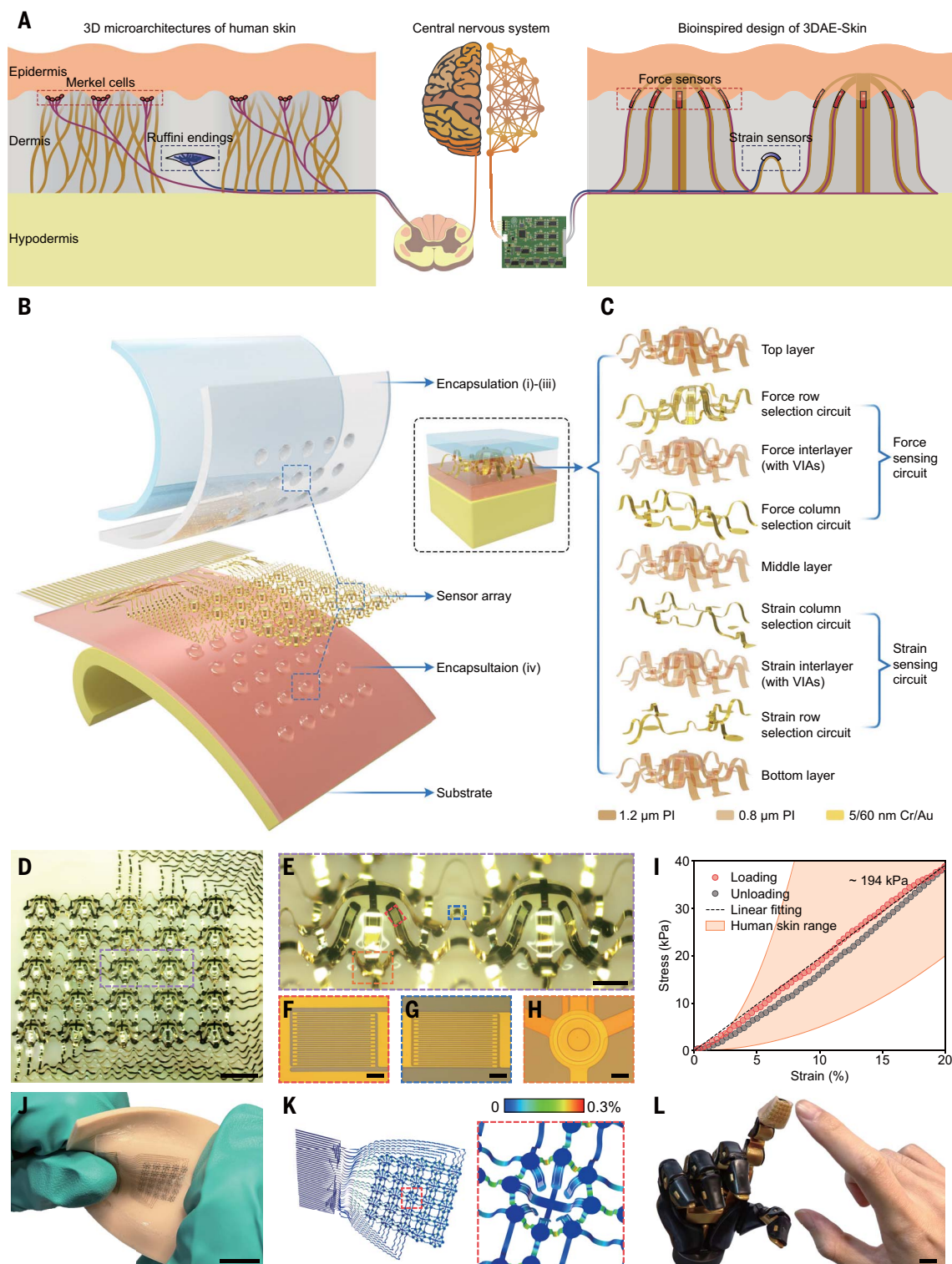†These authors contributed equally to this work.

**Fig. 1. Bioinspired design and fabrication of the 3DAE-Skin.** (**A**) Schematic illustration of the bioinspired design concept of the 3DAE-Skin, which involves a comparison between the architecture of the 3DAE-skin and its artificial tactile system, with that of the skin and tactile system of a human. (**B**) Expanded view of the multilayered construction of an entire 3DAE-Skin device that comprises a sensor array and multiple layers of encapsulation. (**C**) Expanded view of a representative functional unit in which four layers of gold circuits are sandwiched by five layers of PI to form force and strain sensors. (**D**) Image of the interconnected sensor array. Scale bar, 2 mm. (**E**) Enlarged view of the functional unit. Scale bar, 500 μm. (**F** to **H**) Enlarged view of the force sensor (F) and strain sensor (G), as well as bonding site with vertical interconnect access (H). Scale bars, 50 μm. (**I**) Mechanical responses of the 3DAE-Skin under tensile tests, in comparison to those of human skin marked by the orange region. (**J** and **K**) Optical image (J) and FEA results (K) on the deformed configuration of the device being twisted by ~60°, indicating an excellent deformability. The color in (K) represents the maximum principal strain in the gold circuit. (Inset) enlarged view of a functional unit. (**L**) Optical image of the 3DAE-Skin attached to the fingertip of a prosthetic model. Scale bar, 5 mm.

can facilitate the decoding of normal force and directional shear force, according to the outputs of piezoresistive sensors on the different arms. Although the resistive sensors employed in the current study have higher energy consumption and slower response time than piezoelectric or triboelectric sensors, they are better suited to mimic the slow adapting receptors in human skin, as they have the capability to produce continuous signals in response to sustained stimuli [31].

Encapsulation of the functional part with different layers and materials (Fig. 1B, i to iv) yields skin-like mechanical properties. In particular, a heterogeneous encapsulation strategy (Fig. 1B and figs. S8 and S9) leverages capillary forces to allow filling of inner regions of all cage mesostructures with polydimethylsiloxane (PDMS) [Sylgard 184, Dow Corning, Midland, MI, US; mix ratio = 1:15; elastic modulus ~1.5 MPa; encapsulation (iv)], and other regions of the dermis layer with relatively soft material [Ecoflex 00-20, mix ratio = 1:5; elastic modulus ~40 kPa; ~600 μm; encapsulation (iii)]. Introduction of two additional elastomer layers, i.e., Ecoflex 00-20 [mix ratio = 1:1; elastic modulus ~110 kPa; ~120 μm; encapsulation (ii)] and PDMS [Guinie Advanced Materials, Hangzhou, ZJ, China; Elastic modulus ~2 MPa; ~25 μm thick; encapsulation (i)], forms a surface protection (corresponding to the epidermis layer of the 3DAE-Skin) and completes the heterogeneous encapsulation.

Figure 1, D to H, provides optical images of a fabricated 3DAE-Skin and magnified views of the functional unit, force/strain sensors, and vertical interconnect access holes. The device was encapsulated only at the inner regions of cage mesostructures to render improved visual quality. Optical images of the fully encapsulated device (with a total thickness of ~5.25 mm) appear in fig. S10. The cage mesostructure has a lateral dimension of ~1.8 mm, with an arm width of ~250 μm. The encapsulated 3DAE-Skin is very soft, with an effective elastic modulus of ~194 kPa, according to the uniaxial tensile testing (Fig. 1I). The mechanical responses of indentation tests at two typical locations of the 3DAE-Skin appear in fig. S11, from which effective compressive moduli of ~225 kPa and ~119 kPa can be derived. Both the responses of the 3DAE-Skin under uniaxial tension and indentation fall in the typical ranges of human skin responses (Fig. 1I and fig. S11). Because the heterogeneous encapsulation strategy exploits very soft materials to encase the sensors and interconnects, the 3DAE-Skin is also very flexible and stretchable and can be compliantly integrated with the fingertip of a prosthetic hand (Fig. 1, J to L, and movie S1). Finite element analyses (FEA) (see supplementary text for details) can capture complex deformations of 3D mesostructures and strain distributions of metallic layers during various loading conditions (Fig. 1K and fig. S12). According to tensile testing (fig. S13), the maximum uniaxial strain that the 3DAE-Skin can withstand before the failure of its electrical performance is ~45%, corresponding to an effective stress of ~84 kPa.

## Decoupled sensing mechanisms and performances of the 3DAE-Skin

The 3DAE-Skin relies on 3D microarchitecture to convert the external normal/shear force into the strain changes of piezoresistive sensors on the eight-armed cage mesostructure, and then into resistance changes that can be recorded quantitatively. Consider a functional unit that undergoes the loading of a normal force ($F_N$) and a shear force ($F_S$ with an angle of θ with respect to the $x$ axis), as shown in Fig. 2A. Owing the geometric feature of cage mesostructure, the analysis of its static equilibrium (fig. S14) can link normal force ($F_N$) and shear force components ($F_{Sx}$ and $F_{Sy}$) explicitly to the relative resistance changes of eight sensors as

$$F_N = \sum_{i=1}^{8} \left[ S_{(i)} \frac{\Delta R_{(i)}}{\Delta R_{0(i)}} \right] \quad (1)$$

$$F_{Sx} = C \sum_{i=1}^{8} \left[ S_{(i)} \frac{\Delta R_{(i)}}{R_{0(i)}} \cos \frac{(i-1)\pi}{4} \right] \text{ and}$$

$$F_{Sy} = C \sum_{i=1}^{8} \left[ S_{(i)} \frac{\Delta R_{(i)}}{R_{0(i)}} \sin \frac{(i-1)\pi}{4} \right], \quad (2)$$

where $\Delta R_{(i)}/R_{0(i)}$ is the relative resistance change of the $i^{th}$ sensor ($i = 1...8$), $S_{(i)}$ is the sensitivity that can be calibrated using the experiment by only applying a normal force, and $C$ is a dimensionless shape factor that measures the difference of induced strain at the sensors under loadings of only normal and shear forces. Then the total shear force and its loading angle can be given by

$$F_S = \sqrt{F_{Sx}^2 + F_{Sy}^2} \text{ and } \theta = \tan^{-1}(F_{Sy}/F_{Sx}). \quad (3)$$

Optimization of the sensor location in the arm, based on mechanics analyses and FEA enables both a relatively high sensitivity and a large linear range of the force sensing (supplementary text and figs. S15 to S18). Along the thickness direction (total thickness ~4.8 μm), placing the sensor layer at the quarter section point (i.e., 1.2 μm from the top surface) could ensure a reasonably high sensitivity (fig. S19), while avoiding possible failure during microfabrication. The effect of the elastic modulus of the encapsulant inside the cage mesostructure on the sensitivity and linear range is also investigated, showing that a rigid encapsulant can enlarge the linear range but decrease the sensitivity in the meantime, due to the increased mechanical constraint (fig. S19). As such, a moderately rigid material (PDMS, mix ratio = 1:15; elastic modulus ~1.5 MPa) is exploited. The influences of elastic modulus and thickness of other encapsulation/substrate layers are also studied (fig. S20), where the elastic modulus of the encapsulation (iii) plays more evident roles than the other parameters.

Figure 2B shows the sensing performance of the 3DAE-Skin when the sensor array is compressed by a flat indenter, where the pressure denotes the normal reaction force divided by the loading area. The sensitivity to the pressure loading is around $5 \times 10^{-5}$ kPa$^{-1}$, with a linear range of ~80 kPa. Although the encapsulated 3DAE-Skin is quite soft (tensile modulus ~194 kPa), the response is still fast, with a response time of ~0.25 s during a rapid removal of the pressure load (60 kPa). The pressure sensing is stable and reliable during ~3000 cycles of pressure (60 kPa) loading/unloading (Fig. 2C). The wrinkles formed on top of the encapsulated device [due to the introduction of a very thin protective layer (25 μm); see movie S1] have negligible influences on the sensing performance (fig. S21). Although the 3DAE-Skin can endure low-speed compression repeatedly, the reliability under sudden, harsh mechanical impacts could be a concern.

Figure 2, D and E, illustrates the sensing performance of the 3DAE-Skin under shear loadings (applied to a central unit) along different directions. Six different loading angles (θ = 0°, 45°, 112.5°, 180°, 225° and 292.5°) were considered in the experiment, and five shear force magnitudes were applied for each loading angle. The predictions of shear force and loading angle based on Eqs. (2) and (3) agree well with the prescribed values for all the different loading conditions. The sensitivity to the shear force is around $6 \times 10^{-4}$ N$^{-1}$. In comparison to the four-armed mesostructure design [32–34], the eight-armed mesostructure design provides shear deformation information along more in-plane angles, and therefore offers more accurate predictions of shear force and loading angle (fig. S22). For example, the mean absolute errors (0.008 N and 1.5°) of shear force magnitude and angle of eight-armed device are smaller than those (0.030 N and 5.4°) of the four-armed one. A comparison to representative shear sensing devices reported previously (table S2) suggests that our 3DAE-Skin shows one of the minimum levels of mean relative errors.

The sensing of the tensile strain exploits a similar piezoresistive effect and the piezoresistive sensors are arranged on perpendicularly oriented arch mesostructures to sense the strain components along these directions. Figure 2F and fig. S23 suggest a reliable sensing performance during 10,000 cycles of uniaxial stretching (strain amplitude ~20%) applied to
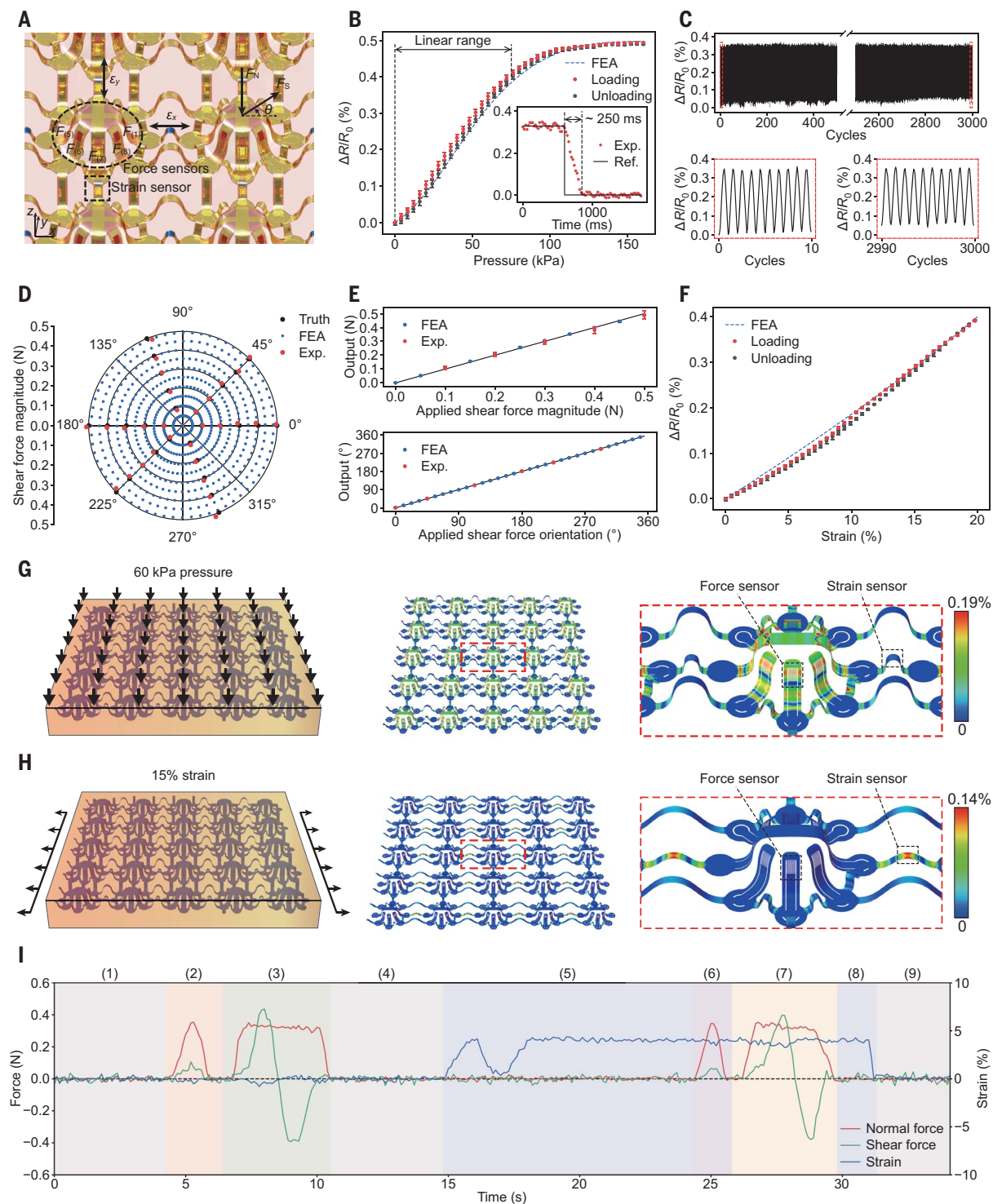
**Fig. 2. Decoupled sensing mechanisms and performances of the 3DAE-Skin.** (**A**) Schematic diagram of the functional unit under typical loadings of normal/shear forces and biaxial tension, where the force and strain sensors are marked. (**B** and **C**) Normal force sensing performance, including the quasistatic response (average relative resistance change of resistance of 8 force sensors) during a loading-unloading cycle (up to ~160 kPa, with a loading rate of 2 kPa/s) (B), the dynamic response under a fast unloading (B, inset), and the loop responses during 3000 cycles of loading and unloading (amplitude ~60 kPa, and frequency ~1 Hz) (C). (**D** and **E**) Shear force sensing performance, including the representation of the force vector in the polar coordinate (D), the response of force magnitudes and orientations when shear forces with different levels and directions are applied, respectively (E). (**F**) Strain sensing performance during a loading-unloading cycle (up to ~20%, with a loading rate of 0.2%/s). (**G**) Distribution of the maximum principal strain in the metal layers of the 3DAE-Skin when the device is under a pressure of 60 kPa. (**H**) Similar results were achieved when the 3DAE-Skin is under a uniaxial stretch of 15%. (**I**) Decoupled responses of the 3DAE-Skin under different types of mechanical loadings. Error bars in (B) and (F) are SD values based on 5 individual measurements.

the 3DAE-Skin, with a sensitivity of ~0.02. All the piezoresistive sensors (240 in total) for force and strain sensing in the fabricated 3DAE-Skin work normally and show quite uniform sensitivity (figs. S24 and S25). Additionally, the temperature rise of these piezoresistive sensors in the 3DAE-Skin is typically very low (below 0.3 K) during operation (fig. S26), and therefore, the associated heating effect on the sensing performance is negligible.

The biomimetic 3D architecture allows decoupled sensing of normal/shear force and tensile strain. Under compressive loading, the maximum principal strain induced in the 3DAE-Skin shows a rapid decay from the loading point. Because the force sensing components are very close to the skin surface and the eight-armed cage mesostructures are much more rigid than the other regions, the maximum principal strains (~0.012%) induced in strain sensing components are much smaller than those (~0.17%) in force sensing components (Fig. 2G for 60 kPa pressure). In this case, the magnitude (~0.012%) of the maximum principal strain in strain sensing components is also much smaller than the value (~0.14%) in strain sensing components under 15% uniaxial stretching. A similar degree of strain difference can be observed under shear loading (fig. S27). Under uniaxial stretching, the maximum principal strains induced in force sensing components are much smaller than those in strain sensing components, owing to the strain isolation of relatively rigid cage mesostructures (Fig. 2H). For example, the peak strain magnitude of force sensing components is only around 0.009% under 15% uniaxial stretching, which is much smaller than the value (~0.17%) under 60 kPa pressure. This set of comparisons illustrates the underlying mechanism of the decoupled sensing capability. Figure 2I and movie S2 provide experimental results during a sequential process of pure pressure loading, coupled loading of pressure and shear force, pure uniaxial stretch, coupled loading of uniaxial stretch and pressure, and coupled loading of stretch, pressure, and shear force. The responses of normal/shear forces and strain quantitatively demonstrate the decoupled sensing capability of the 3DAE-Skin. Additionally, the characterization of strain and shear force sensing was performed under pressure values of 0, 20, and 40 kPa (fig. S27), where slight influences of applied pressure can be observed, providing further evidence of the decoupled sensing capability.

### Spatiotemporal mapping of normal/shear forces and strain

The 3DAE-Skin is integrated with the data acquisition circuit and signal processing module to form a tactile system (Fig. 3A, figs. S28 to S30, and table S3). The data acquisition circuit allows individual addressing of each piezoresistive sensor in the array without crosstalk (Fig. 3B) (with ~50 kS/s sampling rate and 16-bit resolution). Based on the temporal relative resistance change of all 240 piezoresistive sensors in the 3DAE-Skin, the signal processing module allows visualization of the spatiotemporal distribution of normal/shear forces and strain according to Eqs. (1) to (3), and quantitative decoding of the tactile information (e.g., the location of the applied force, the elastic modulus, and local principal curvature components of an object) through a deep learning neural network (DNN) model. A spatiotemporal map (fig. S31) is introduced to visualize the distributions of sensed normal/shear forces and strain, in which 25 colored octagons are exploited to represent force responses, with the color (or size) of each octagon denoting the magnitude of normal force and the black arrow (or distortion of each octagon) denoting the magnitude and direction of shear force. The horizontal and vertical spacings between adjacent octagons represent the normal strain components along the two directions. The red-dotted octagon is the baseline in the force-free state and the strain magnitude is magnified by 10 times for a better visualization. Figure 3, C to G, and movie S3 provide experimental results of spatiotemporal variations in normal/shear forces and strain, when the 3DAE-Skin touches three 3D-printed relief structures (i.e., letters T, H and U) (0.5 mm in thickness and 8 mm in lateral dimension; 1.75 GPa; see fig. S32 for details). Figure 3D presents the time histories of pressure and shear force components at the 9 units in the central region, and strain responses at the adjacent 12 units. The responses of all force/strain units are provided in figs. S33 and S34, and the raw data of relative resistance change in the 10 piezoresistive sensors of a typical unit are in fig. S35. Figure 3, E to G, shows the spatiotemporal maps at three typical moments ($t$ = 13.9 s, 25.9 s, and 34.4 s). When the 3DAE-Skin is pressed on the T-shaped relief structure through a non-uniform compression, the spatial distribution of the pressure is captured (Fig. 3E). When both normal and shear forces are applied during the interaction, tensile strains are induced at one side of the 3DAE-Skin (Fig. 3F), noting that the relief structure is much more rigid than the 3DAE-Skin. The last example in Fig. 3G corresponds to a complex loading condition in which a spatially non-uniform shearing coupled with pressing is applied. The spatially varying directions of the arrows serve as evidence that the coupled normal/shear forces could be well-measured in various units of the 3DAE-Skin. Additionally, the torque applied to the letter "U" is well correlated with spatially directed arrows of relevant units (Fig. 3G), indicating the potential of the 3DAE-Skin in torque sensing.

Super-resolution sensing (35, 36) of the 3DAE-Skin–based tactile system is made possible by incorporating a DNN model (see supplementary text for details) that establishes the implicit mapping between the location and magnitude of an applied normal force and relative resistance changes of 240 piezoresistive sensors in the 3DAE-Skin (Fig. 3, H to J, figs. S36-S38, and table S4). With aid of the DNN model, the prediction accuracy of loading position has been substantially improved, in comparison to the case of the linear interpolation (fig. S39). An evident reduction (from 1.086 mm to 0.117 mm) of the root-mean-square error can be observed. Such a resolution (0.117 mm) of the normal force sensing is very close to the resolution of force sensing by human hands (37–39). In the condition of combined normal and shear force loadings, the utility of DNN model can also enable a super-resolution sensing, as evidenced by the improved prediction accuracy of loading position (fig. S40 and table S5).

A comparison of the performance/capability (table S6) among state-of-art electronic skins and real human skin shows the advancement of the proposed 3DAE-Skin, especially in the decoupled perception of normal force, shear force and strain. Such fully decoupled mechanosensation is challenging to achieve, based on electronic skins with 2D structural layouts (fig. S41) or other designs reported previously (table S6).

### Simultaneous quantitative measurements of elastic modulus and principal curvature components

Quantitative measurements of an object's elastic modulus and principal curvature components are pivotal for applications of prosthetic hands (31, 40, 41) as object shape is unknown in many practical situations. When touching an object, human fingertips usually rely on the sensed force distribution and its own skin deformation to infer the softness and local shape of the object. Similarly, the 3DAE-Skin–based tactile system can distinguish the softness of two objects through different levels of induced strains in the 3DAE-Skin and identify the local curvature through different normal/shear force distributions (e.g., Fig. 4A). Development of a DNN model (see supplementary text for details) that correlates the elastic modulus ($E$) and principal curvature components ($\kappa_1$ and $\kappa_2$) with relative resistance changes of 240 piezoresistive sensors allows prediction of the elastic modulus of an object without knowing its shape. The dataset was constructed based on a diversity of samples with 51 different surface shapes (ellipsoidal, spherical, cylindrical, and planar) and 15 different moduli (from 40 kPa to 3.9 MPa) (figs. S42 to S44 and tables S7 and S8). The data consisted of 30,600 samples that were split into datasets
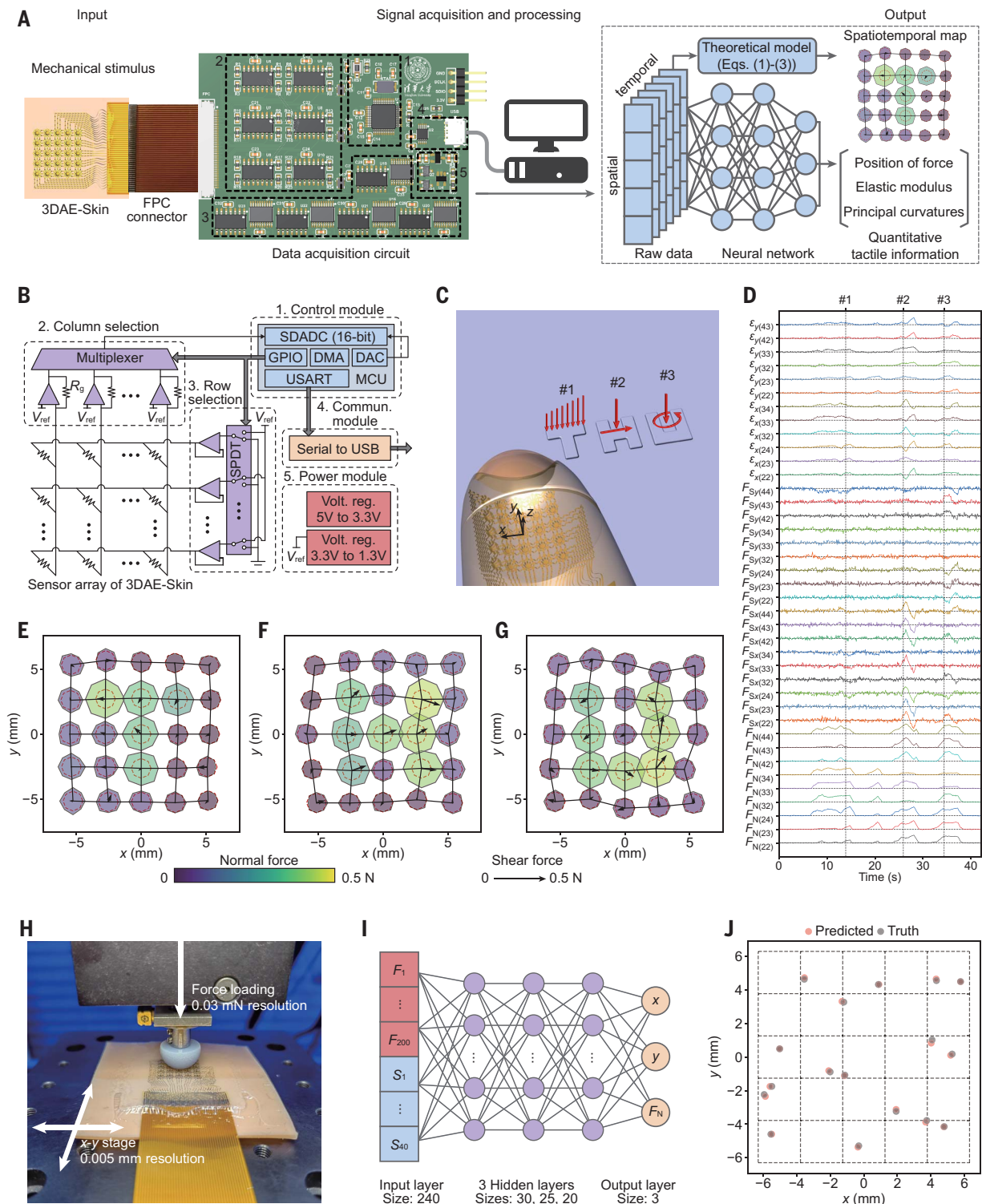
**Fig. 3. Spatiotemporal mapping of forces and strain using the 3DAE-Skin–based tactile system.** (**A**) Schematic illustration and working mechanism of the 3DAE-Skin–based haptic system. The black dashed boxes in the photo of the PCB indicate different components of the circuit: (1) control module; (2) column selection module; (3) row selection module; (4) communication module; (5) power module. A separate computer is utilized for DNN training and testing. (**B**) Block diagram of the data acquisition circuit in which the number of each module indicates the corresponding labeled component in (A). (**C**) Schematic illustration of the test of the spatiotemporal mapping in which artificial finger with integrated 3DAE-Skin touched the three letters of "THU" with different loading modes. (**D**) Temporal recordings of typical signals during the test in (C), including pressure and shear force (both x- and y-axis) signals from 9 selected units and strain signals from 12 selected units. (**E** to **G**) Visualization of the tactile sensation at three moments of the test shown in (C). (**H**) Optical image of the experimental setup used to collect data for realizing the spatial super-resolution of pressure sensing aided by deep learning. (**I**) Schematic diagram of the DNN model for the super-resolution sensing. F, force sensor; S, strain sensor. (**J**) Prediction results of loading positions by the trained DNN model on a part of the test set.
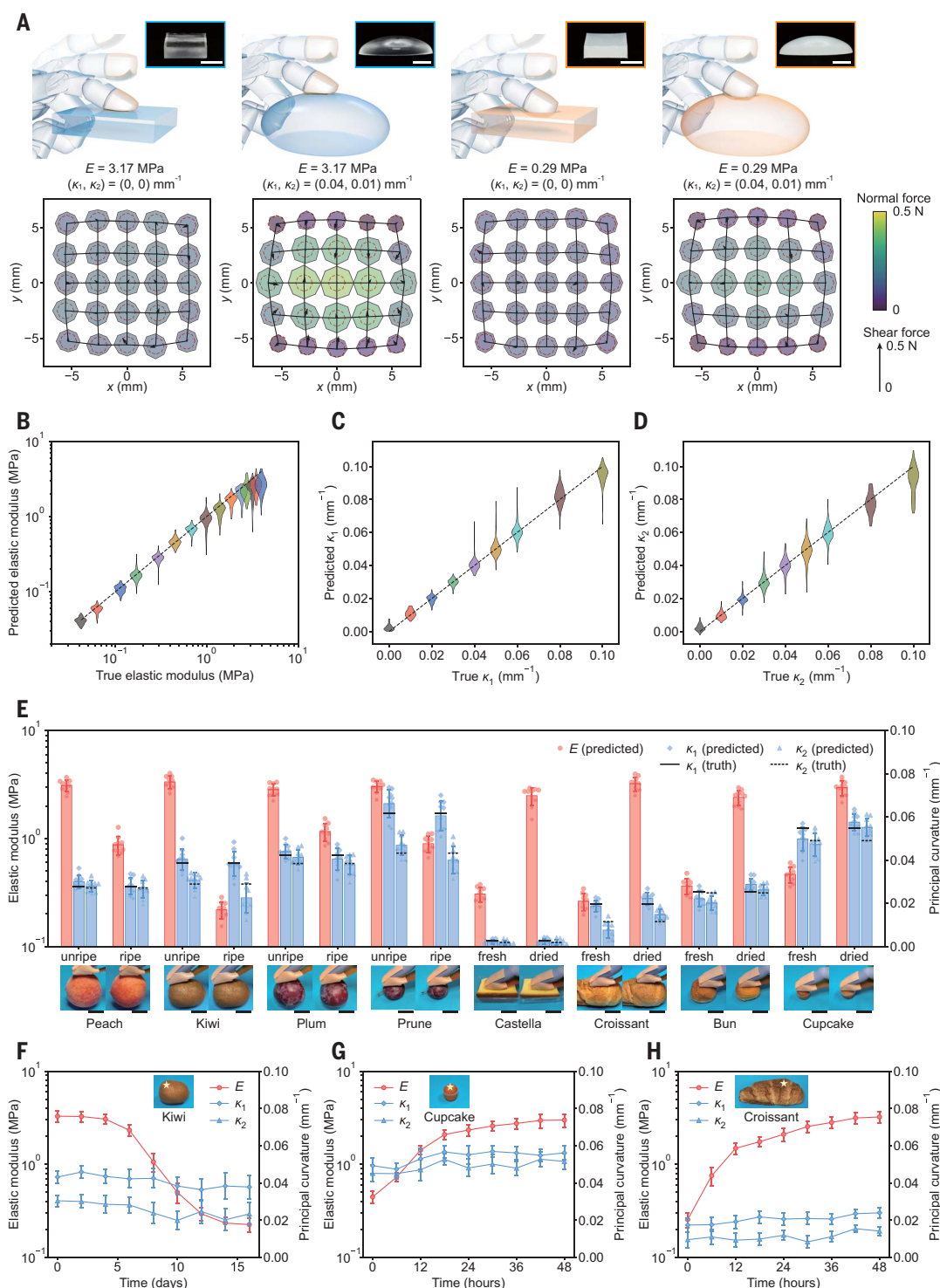
**Fig. 4. Simultaneous quantitative measurements of elastic modulus and principal curvature components.** (**A**) Visualized tactile information when the 3DAE-Skin contacts four standard samples with different combinations of elastic modulus ($E$) and surface shape characterized by the principal curvature components ($\kappa_1$ and $\kappa_2$). The first row shows the schematic illustrations with optical images of real samples as insets (scale bars, 2.5 cm). The second row shows the corresponding spatiotemporal maps. The normal resultant force is fixed at around 0.5 N during those tests. (**B** to **D**) Testing results of elastic modulus and principal curvature components based on the developed tactile system. A total of 765 samples with various elastic moduli and surface shapes were tested experimentally to construct the dataset.

(**E**) Simultaneous measurements of elastic modulus and principal curvature components of eight different foods, including four kinds of fruits (peach, kiwi, plum, and prune), each with distinct levels of ripeness, and four kinds of bread/cake (castella, croissant, bun, and cupcake) in both fresh and dried conditions. Scale bars, 4 cm. The ground truths of principal curvature components are denoted by solid black line (for $\kappa_1$) and black dash line (for $\kappa_2$), respectively. (**F** to **H**) Long-term monitoring of the elastic modulus and principal curvatures of (F) kiwi, (G) cupcake, and (H) croissant left in air for 16, 2, and 2 days, respectively. The stars denote the regions touched by the 3DAE-Skin. The average values of 5 independent predicted results are shown with SD values.

of training, validation, and testing with a ratio of around 8:1:1. The use of DNN model ensures more accurate predictions than other classical machine-learning models such as linear regression, KNN regression, and random forest regression models (fig. S45). Figure 4, B to D, shows testing results of 2700 samples from the testing set, where reasonably good predictions of the elastic modulus can be observed in the range of 40 kPa to 3.9 MPa, for a number of differently shaped objects. Similar to human skin, the 3DAE-Skin–based tactile system can measure the modulus values that are comparable to its own effective tensile modulus (~194 kPa). When the elastic modulus (e.g., > 1 MPa) of the target object is much higher than the 3DAE-Skin modulus, the target object barely deforms during the interaction, leading to a reduction of the prediction accuracy as compared with the cases when $E$ is close to 194 kPa. Owing to the relatively small spacing (2.5 mm) of the force sensing units, the 3DAE-Skin–based tactile system can provide reasonably good predictions of local curvature components when they are up to around 0.1 mm$^{-1}$. Videos showing simultaneous modulus and curvature measurements of eight selected samples are presented in movie S4. Reducing the number of operational sensors in the 3DAE-Skin leads to an increase of the mean relative error of modulus prediction (fig. S46).

The ripeness or freshness of some food (e.g., kiwi, peach, cake, and bread) is challenging to distinguish using image recognition or other computer vision methods (42–44). The 3DAE-Skin–based tactile system presented could provide a possible rapid solution through touch. We measured the elastic moduli of four fruits (kiwi, peach, plum, and prune, with the principal curvature components ranging from ~0.02 to ~0.07 mm$^{-1}$) in both unripe and ripe states (Fig. 4E and movies S5 and S6). Fruit shape changes very slightly during ripening, but it gradually becomes softer during this process. For example, the modulus of the kiwi decreases slightly in the first 6 days and then rapidly until the kiwi is overripe at day 14 (Fig. 4F). The modulus (~0.2 MPa) of the ripe kiwi (day 14) is an order of magnitude lower than that (~3.2 MPa) of the unripe kiwi (day 0). Similarly, the modulus (~0.9 MPa) of the ripe peach (day 14) is also much smaller than that (~3.1 MPa) of the unripe peach (day 0). By contrast, fermented bread or cake tends to become more rigid during long-term air exposure, as a result of drying-induced hardening. Figure 4G shows that the modulus of the cupcake increases rapidly (from ~0.45 MPa to ~2.3 MPa) during the first day and relatively slowly (to ~3.0 MPa) during the following day, because the dehydration is mostly complete in the first 24 hours. The croissant shows more significant hardening (from ~0.3 MPa to ~3.3 MPa).

## Conclusions

The bioinspired 3D architected designs, heterogeneous encapsulation strategies, and microfabrication technologies allow for the development of 3DAE-Skin that mimics the spatial arrangement of Merkel cells and Ruffini endings in human skin, as well as the skin's multilayer geometrical/mechanical characteristics. Such bioinspired designs leverage the 3D distribution of force and strain sensing components and the engineered stiffness variations in E-Skin to achieve decoupled sensing of normal/shear forces and tensile strains. Integration of the 3DAE-Skin with data acquisition/processing modules aided by deep learning algorithms allows development of a tactile system capable of normal/shear force sensing with spatial resolution comparable to human skin, as well as simultaneous modulus and curvature measurements through a simple touch of an object. Demonstrations on the modulus measurement of fruits, bread, and cake with diverse shapes suggest applications in the assessment of the food whose rigidity changes with time. The capabilities to quantitatively assess the contact state and the object information in real time also have important implications for human-machine interactions, humanoid robots, smart prostheses, and auto inspection instruments. For example, by measuring friction coefficients between the device and different target objects, the 3DAE-Skin system can potentially distinguish a rough surface from a smooth one (fig. S47). Although the presented 3DAE-Skin is developed to imitate the perception of fingertip, the design and fabrication methods are scalable and can be extended for uses in other types of prosthetic/robotic systems. Further improvements in the cell density of 3DAE-Skin can be achieved by reducing the structural dimensions of the 2D precursor design and increasing the magnitude of biaxial prestrain used in the 3D assembly (fig. S48), noting that there should be a limit considering the resolution of photolithography.

## REFERENCES AND NOTES

1. A. Zimmerman, L. Bai, D. D. Ginty, *Science* **346**, 950–954 (2014).
2. A. Handler, D. D. Ginty, *Nat. Rev. Neurosci.* **22**, 521–537 (2021).
3. R. S. Johansson, J. R. Flanagan, *Nat. Rev. Neurosci.* **10**, 345–359 (2009).
4. A. Iggo, A. R. Muir, *J. Physiol.* **200**, 763–796 (1969).
5. S. M. Maricich et al., *Science* **324**, 1580–1582 (2009).
6. M. R. Miller, H. J. Ralston 3rd, M. Kasahara, *Am. J. Anat.* **102**, 183–217 (1958).
7. M. R. Chambers, K. H. Andres, M. von Duering, A. Iggo, *Q. J. Exp. Physiol. Cogn. Med. Sci.* **57**, 417–445 (1972).
8. D. H. Kim et al., *Science* **333**, 838–843 (2011).
9. S. Lee et al., *Science* **370**, 966–970 (2020).
10. B. C. K. Tee et al., *Science* **350**, 313–316 (2015).
11. Y. Kim et al., *Science* **360**, 998–1003 (2018).
12. W. W. Lee et al., *Sci. Robot.* **4**, eaax2198 (2019).
13. W. Wang et al., *Science* **380**, 735–742 (2023).
14. S. Xu et al., *Science* **344**, 70–74 (2014).
15. H. U. Chung et al., *Science* **363**, eaau0780 (2019).
16. D. Jung et al., *Science* **373**, 1022–1026 (2021).
17. S. Wang et al., *Nature* **555**, 83–88 (2018).
18. T. Sekitani et al., *Science* **326**, 1516–1519 (2009).
19. Z. F. Liu et al., *Science* **349**, 400–404 (2015).
20. C. M. Boutry et al., *Nat. Electron.* **1**, 314–321 (2018).
21. C. M. Boutry et al., *Sci. Robot.* **3**, eaau6914 (2018).
22. G. Li, S. Liu, L. Wang, R. Zhu, *Sci. Robot.* **5**, eabc8134 (2020).
23. I. You et al., *Science* **370**, 961–965 (2020).
24. Y. Yu et al., *Sci. Robot.* **5**, eaaz7946 (2020).
25. K. Yao et al., *Nat. Mach. Intell.* **4**, 893–903 (2022).
26. Y. Yu et al., *Sci. Robot.* **7**, eabn0495 (2022).
27. J. Kim et al., *Nat. Commun.* **5**, 5747 (2014).
28. S. Xu et al., *Science* **347**, 154–159 (2015).
29. Y. Zhang et al., *Nat. Rev. Mater.* **2**, 17019 (2017).
30. X. Cheng et al., *Science* **379**, 1225–1232 (2023).
31. A. Chortos, J. Liu, Z. Bao, *Nat. Mater.* **15**, 937–950 (2016).
32. S. M. Won et al., *ACS Nano* **13**, 10972–10979 (2019).
33. M. Han et al., *Nat. Biomed. Eng.* **4**, 997–1009 (2020).
34. J. W. Kwak et al., *Sci. Transl. Med.* **12**, eabc4327 (2020).
35. Y. Yan et al., *Sci. Robot.* **6**, eabc8801 (2021).
36. H. Sun, G. Martius, *Sci. Robot.* **7**, eabm0608 (2022).
37. K. O. Johnson, J. R. Phillips, *J. Neurophysiol.* **46**, 1177–1192 (1981).
38. H. E. Wheat, A. W. Goodwin, A. S. Browning, *J. Neurosci.* **15**, 5582–5595 (1995).
39. M. Hollins, S. R. Risner, *Percept. Psychophys.* **62**, 695–705 (2000).
40. E. D'Anna et al., *Sci. Robot.* **4**, eaau8892 (2019).
41. S. Raspopovic, G. Valle, F. M. Petrini, *Nat. Mater.* **20**, 925–939 (2021).
42. D. Barik, M. Mondal, in *2010 2nd International conference on education technology and computer* (IEEE, 2010), vol. 2, pp. V2-170–V172.
43. H. Guan, J. Zhang, in *2016 IEEE International conference on robotics and biomimetics (robio)* (IEEE, 2016), pp. 1685–1690.
44. G. Tatiya, J. Sinapov, in *2019 International conference on robotics and automation (ICRA)* (IEEE, 2019), pp. 7872–7878.

## SUPPLEMENTARY MATERIALS

science.org/doi/10.1126/science.adk5556
Materials and Methods
Supplementary Text
Figs. S1 to S48
Tables S1 to S8
References (45–60)
Movies S1 to S6